High figure of merit Magneto-optical Ce and Bi-substituted Terbium Iron Garnet films integrated on Si

Takian Fakhrul, Stana Tazlaru, Bharat Khurana, Lukáš Beran, Jackson Bauer, Michal Vančík, Ariane Marchese, Ekaterina Tsotsos, Miroslav Kučera, Yan Zhang, Martin Veis, Caroline A. Ross**

T. Fakhrul, Bharat Khurana, Jackson Bauer, A. Marchese, E. Tsotsos, Yan Zhang, Prof. C. A. Ross

Department of Materials Science and Engineering

Massachusetts Institute of Technology

Cambridge, MA, 02139, USA

E-mail: takianf@mit.edu ; caross@mit.edu

S. Tazlaru, L. Beran, M. Vančík, M. Kučera, Prof. M. Veis

Faculty of Mathematics and Physics

Charles University

Ke Karlovu 3, 12116 Prague 2, Czech Republic

Y. Zhang

Engineering Research Center of Electromagnetic Radiation Control Materials

University of Electronic Science and Technology of China

Chengdu 610054, China

Abstract

This is the author manuscript accepted for publication and has undergone full peer review but has not been through the copyediting, typesetting, pagination and proofreading process, which may lead to differences between this version and the Version of Record. Please cite this article as doi: 10.1002/adom.202100512.

Films of polycrystalline terbium iron garnet (TbIG), cerium substituted TbIG (CeTbIG) and bismuth substituted TbIG (BiTbIG) were grown on Si substrates by pulsed laser deposition. The films grow under tensile strain due to thermal mismatch with the Si substrate, resulting in a dominant magnetoelastic anisotropy which, combined with shape anisotropy, leads to in-plane magnetization. TbIG has a compensation temperature of 253 K which is reduced by substitution of Ce and Bi. The Faraday rotation at 1550 nm of the TbIG, $Ce_{0.36}$TbIG and $Bi_{0.03}$TbIG films were 5400 ± 600 °/cm, 4500± 100 °/cm and 6200± 300°/cm respectively while $Ce_{0.36}$TbIG and $Bi_{0.03}$TbIG exhibited lower optical absorption than TbIG, attributed to a reduction in Fe^{2+} and Tb^{4+} absorption pathways. The high Faraday rotation of the films, and in particular the high magnetooptical figure of merit of the $Bi_{0.03}$TbIG of 720 °dB^{-1} at 1550 nm, make these polycrystalline films valuable for applications in integrated photonics.

Keywords: Rare-earth iron garnets, magneto-optical, optical absorption, Faraday rotation, figure of merit

Introduction

Magnetooptical (MO) materials provide nonreciprocal functionality in optical circuits and networks. In particular, optical isolators based on nonreciprocal mode conversion or phase shift are key components of optical networks, ensuring unidirectional propagation of light.[1-6] The nonreciprocity of a MO material is given by the off-diagonal terms of the permittivity tensor, and can be characterized by measuring the Faraday rotation. For the near-IR optical communications bands, materials based on ferrimagnetic yttrium iron garnet (YIG, $Y_3Fe_5O_{12}$) offer a desirable combination of a high Faraday rotation and a low optical absorption. Cerium- and bismuth-substituted yttrium iron garnet (CeYIG, BiYIG) have an excellent MO figure of merit (FoM, the ratio of Faraday rotation to optical absorption),[3-18] and bismuth iron garnet and paramagnetic terbium gallium garnet are both used in bulk optical isolators.

In order to incorporate these complex oxides into photonic integrated circuits, films with high FoM must be grown onto photonic substrates and devices. Although YIG crystallizes readily on non-garnet substrates, it has a low Faraday rotation (~ +100 °/cm at 1550 nm)[10] and FoM. Crystallization of CeYIG or BiYIG without secondary phases can be accomplished by depositing then annealing the film directly or by annealing a bilayer consisting of a YIG seedlayer placed either above or below the active MO layer.[12,13,18] When a seed layer is included, a top seed layer is preferable as it maximizes coupling of the MO garnet with an optical mode propagating through an underlying waveguide.

Like YIG, rare earth garnets such as terbium iron garnet (TbIG) or dysprosium iron garnet [19,20] can crystallize directly on non-garnet substrates to form polycrystalline films. TbIG is a thermodynamically stable phase [21,22] which promotes garnet-phase crystallization without a

seed layer. TbIG has a Faraday rotation in the 1100 – 1550 nm wavelength range of ~ +270 to +1000 °/cm. [23-25] Bi-substituted TbIG has been grown by liquid-phase epitaxy and flux methods[23-27] or sol-gel methods [28], and more recently thin films of Ce- and Bi-substituted TbIG (CeTbIG, BiTbIG) were grown on Si by sputtering.[29-34] Sputtered BiTbIG with Bi substitution of 14% of the Tb sites has a Faraday rotation of ~ -500 °/cm at 1550 nm,[29] the same sign as that of CeYIG, which at 1550 nm wavelength had a Faraday rotation of at least -3700 °/cm.[30] CeTbIG films with Ce substituting up to 25% of the Tb sites showed a Faraday rotation above -3200 ± 200 °/cm,[31,32] but a 44 nm thick magnetic dead layer formed between the waveguide and the CeTbIG, hindering the interaction of evanescent light with the MO garnet cladding.[32] However, the optical absorption and FoM of these Bi- and Ce-substituted TbIG materials has not yet been reported.

In this paper we report the growth, magnetic and optical characteristics of polycrystalline thin films of TbIG, CeTbIG and BiTbIG synthesized using pulsed laser deposition (PLD) on Si substrates. The effect of the growth conditions on the stoichiometry of TbIG, CeTbIG and BiTbIG films is discussed. We show that by composition control of the Ce- and Bi-substituted TbIG, high Faraday rotation is achievable, up to 6200 °/cm at 1550 nm wavelength. The optical absorption of the TbIG garnet films can be reduced by addition of Bi^{3+} and Ce^{3+} and the possible mechanisms of optical absorption in these films are discussed. The figure of merit reached 720 °/dB, the highest reported for polycrystalline garnet films with the added benefit of improved device performance due to the absence of a seed layer. The temperature dependence of the magneto-optical and magnetic properties of these thin films are also characterized.

2. Results

2.1. Structural, Compositional and Surface Characterization of TbIG/Si, CeTbIG/Si and BiTbIG/Si

TbIG, CeTbIG and BiTbIG films were grown on Si substrates with native oxide by PLD as described in the Experimental Methods by codeposition from $Tb_3Fe_5O_{12}$, $Ce_1Tb_2Fe_5O_{12}$ and $Bi_{0.3}Tb_{2.7}Fe_5O_{12}$ targets. Iron garnets such as $Tb_3Fe_5O_{12}$ form cubic crystals with lattice parameter of ~1.2 nm and 8 formula units per unit cell, illustrated in Figure 1a. Tb, Bi and Ce are expected to occupy 3 dodecahedral sites per formula unit whereas the Fe occupies 2 octahedral and 3 tetrahedral sites. We define a composition parameter R as the ratio of $\frac{Tb+Ce+Bi}{Fe}$ which characterizes how close the film is to the ideal cation stoichiometric ratio of R=0.6. Table S1 in the supplementary material shows the cation ratios of films made in this study determined by wavelength dispersive x-ray spectroscopy (WDS).

Figure 1b-d shows the x-ray diffraction (XRD) patterns and R ratios for several samples of TbIG, CeTbIG and BiTbIG after rapid thermal annealing (RTA) at 900 °C for 3 min. The nominally TbIG samples have an R ratio of 0.70, 0.57 and 0.54 (Figure 1b), yet they each crystallize well on Si, showing the characteristic garnet (400), (420) and (422) powder peaks near 2θ = 30° with no

detectable peaks from secondary phases. An iron deficiency similar to that of the TbIG with R=0.70 has also been reported for single crystal TbIG films with the excess Tb incorporated into the octahedral sites usually occupied by Fe [35]. The iron deficiency of the films in this study was reduced by using a lower laser fluence which is believed to result in less scattering of Fe atoms in the PLD plume compared to the rare earth.

In the case of CeTbIG, while all the compositions shown in Figure 1c form garnet phases, only the $Ce_{0.36}$TbIG film, which has a R ratio that is closest to 0.6, crystallizes with all three of the garnet peaks near 2θ = 30˚. Increasing Ce content led to the formation of broad garnet peaks or secondary phase formation. For BiTbIG, most of the films have very low bismuth content compared to the target. This is due to the volatility of bismuth, which is commonly depleted during high temperature deposition or annealing.[12] By using a lower substrate temperature of 700 ˚C and a higher oxygen pressure of 100 mTorr, the Bi content was greatly enriched, forming $Bi_{0.79}$TbIG with a R ratio of 0.66, but this composition did not crystallize as a single phase garnet according to the XRD data (Figure 1d).

Based on the structural and compositional analysis we selected three exemplary films for further magnetic and magneto-optical characterization. The films, of composition TbIG (123 nm thick, measured composition Tb:Fe = 2.9:5.1, R=0.57), $Ce_{0.36}$TbIG (72 nm, Ce:Tb:Fe = 0.36:2.59:5.05, R = 0.58) and $Bi_{0.03}$TbIG (79.8 nm, Bi:Tb:Fe = 0.03:3.06:4.9, R = 0.63), consist of polycrystalline single-phase garnet. AFM images of these three films in Figure 2(a-c) and supplementary Figure S1(a-c) show that the TbIG has a grain size of the order of 100 – 150 nm, the CeTbIG exhibits a range of grain sizes from 20 - 100 nm, and the $Bi_{0.03}$TbIG had a grain size of 10-30 nm with the grains forming larger clusters. Even though the final Bi content in the film is small, we expect that the film contained a much greater fraction of Bi prior to RTA which was lost on annealing, and this affected the microstructural development compared to that of TbIG.

2.2. Magnetic Characterization

Magnetic hysteresis of the films was measured with the magnetic field applied both in-plane and out-of-plane (perpendicular to the films) using a vibrating sample magnetometer (VSM), and temperature-dependent in-plane magnetic hysteresis measurements were carried out using a SQUID magnetometer. The VSM hysteresis loops at room temperature are given in Figure 2d-f. The TbIG (R=0.57), $Ce_{0.36}$TbIG and $Bi_{0.03}$TbIG films have room temperature saturation magnetization (M_s) of 43, 26 and 38 kA m^{-1} respectively. The total anisotropy of the films includes the sum of magnetocrystalline, magnetoelastic (K_{me}) and shape (K_{sh}) anisotropy contributions. The magnetocrystalline anisotropy can be neglected due to the polycrystallinity of the films, and the net uniaxial anisotropy becomes

$$K_u = K_{me} + K_{sh} = -\frac{3}{2}\lambda\frac{\mathrm{E}}{1-\nu}(\varepsilon_z - \varepsilon_x) - \frac{\mu_o}{2}M_s^2 \qquad (1)$$

where λ is the magnetostriction coefficient for the polycrystal, E is the Young's modulus, ν is the Poisson's ratio and ε_x and ε_z are the in-plane and out-of-plane strain. Iron garnet is close to being elastically isotropic, with an elastic anisotropy factor $2c_{44}/(c_{11} + c_{12}) = 0.947$ calculated for YIG [36] where c_{11}, c_{12}, and c_{44} are the three independent cubic elastic constants. The elastic properties of polycrystalline garnet are then given by $E = \frac{(c_{11}+2c_{12})(c_{11}-c_{12})}{(c_{11}+c_{12})}$ and $\upsilon = \frac{c_{12}}{c_{11}+c_{12}}$. The room temperature magnetostriction coefficients of single crystal TbIG are $\lambda_{100} = -3.3 \times 10^{-6}$ and $\lambda_{111} = +12 \times 10^{-6}$ [37]. The approximation for the magnetostriction λ of a polycrystal proposed by Akulov[38] is

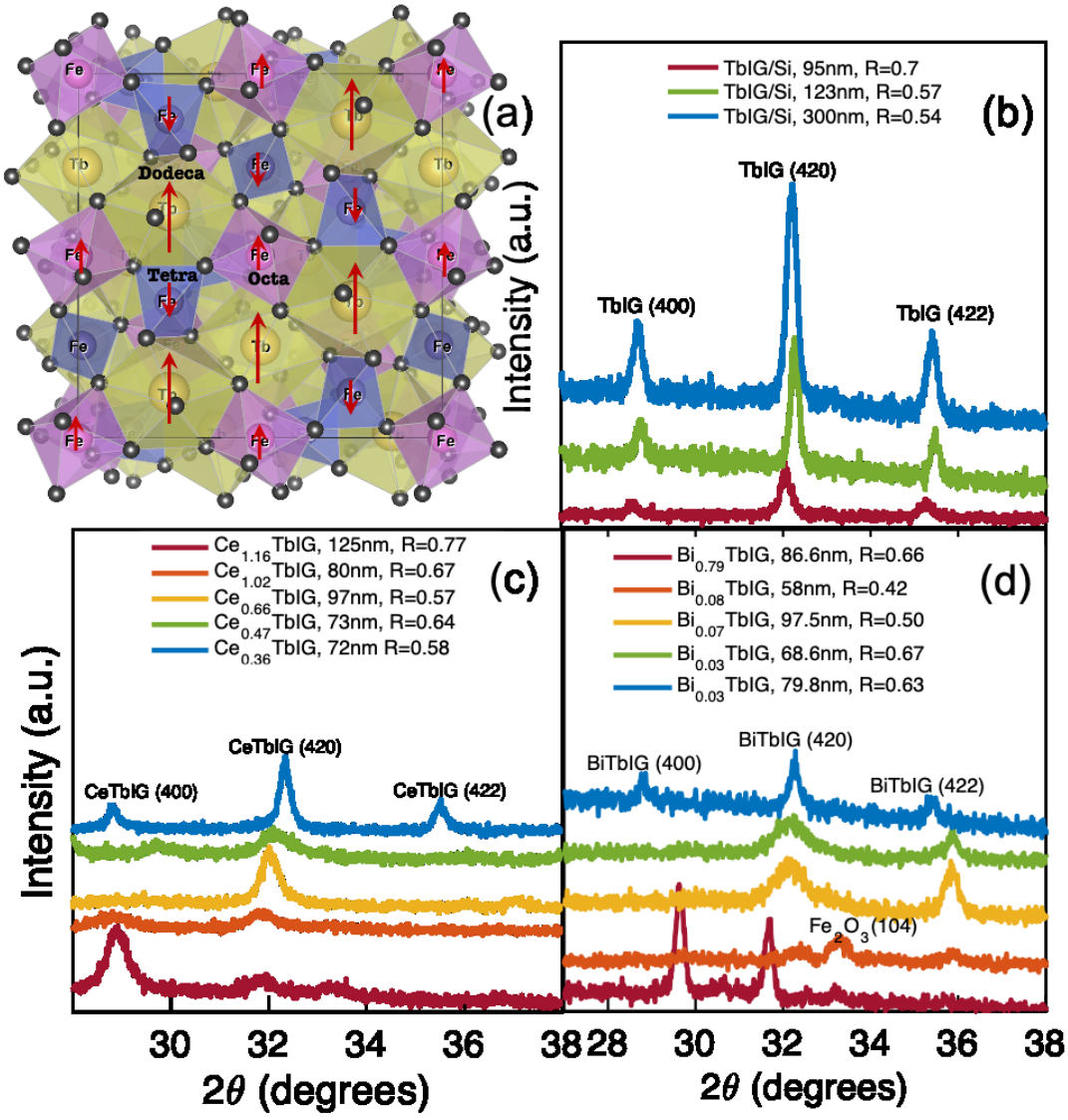

Figure 1. (a) Cubic unit cell of TbIG showing octahedral (pink), tetrahedral (purple) and dodecahedral (yellow) sites. The cation sites are surrounded by O^{2-} (indicated by black spheres) at the vertices of the polyhedrons. Magnetization directions of the Tb^{3+} and Fe^{3+} cations are shown using red arrows. (b-d) XRD ω–2θ scans for polycrystalline (a) TbIG , (b) CeTbIG and (c) BiTbIG films on silicon after RTA at 900°C for 3min.

$$\lambda = \frac{2}{5}\lambda_{100} + \frac{3}{5}\lambda_{111} \quad (2)$$

which yields $\lambda = +5.88 \times 10^{-6}$ for TbIG. An approximation of Callen and Goldberg[39,40] which assumes a non-uniform mechanical stress within the polycrystalline aggregate gives a similar result of $\lambda = +5.73 \times 10^{-6}$ based on the elastic constants of TbIG.[38]

The strain state in the garnet films on Si is dominated by thermal expansion mismatch. The in-plane strain is $\varepsilon_x = \varepsilon_y = \varepsilon_o = \Delta\alpha\Delta T$ where $\Delta\alpha = \alpha_{film} - \alpha_{substrate}$ is the mismatch between the thermal expansion coefficient (α) of the film and substrate and ΔT is the temperature change. We assume for TbIG that α has little variation within the temperature range, which is a reasonable approximation for iron garnets.[41] The TbIG film on Si will experience an in-plane tensile strain after cooling down from 900 °C. For an isotropic film under biaxial stress, the out-of-plane strain is $\varepsilon_z = -\frac{2\nu}{1-\nu}\varepsilon_o$.

Both magnetoelastic and shape anisotropy favor an in-plane easy axis, though the magnetoelastic contribution for TbIG (R=0.57) is more than 2 times greater than the shape anisotropy. The total anisotropy for the films, K_u, is calculated from the predicted thermal mismatch, magnetostriction and magnetization and is shown in Table 1. The values of K_u have the same sign and indicate an in-plane easy magnetization direction for all the films. The calculated anisotropy for TbIG (R=0.57) agrees well with the anisotropy determined experimentally from the difference in area between the in-plane and out-of-plane anhysteretic loops (i.e. the measured loops with hysteresis subtracted) [40], suggesting that thermal mismatch provides a reasonable estimation of the strain state and the bulk magnetostriction values are appropriate.

In contrast, the measured anisotropy of the $Bi_{0.03}$TbIG is 5 times higher than that of the TbIG, exceeding the value predicted from the magnetostriction and thermal mismatch strain. This suggests that the strain or the magnetostriction are higher than those of TbIG, or there may be another source of anisotropy. The magnetostriction is likely similar to that of TbIG due to the small Bi content, but Bi loss on annealing and the subsequent volume reduction could account for an increase in the in-plane tensile strain, and the Bi may also affect strain relaxation mechanisms.[42]

The magnetostriction of Ce-substituted garnets is not well characterized, but magnetostriction coefficients of $\lambda_{100} = +120 \times 10^{-6}$ and $\lambda_{111} = +50 \times 10^{-6}$ [43-45] have been extrapolated for the theoretical garnet $Ce_3Fe_5O_{12}$ based on data from YIG with small substitutions of Ce. Ce provides a positive contribution to the magnetostriction of YIG, and extrapolating from data reported by Wijn[43] we estimate $\lambda = +35\ 10^{-6}$ for polycrystalline $Ce_{0.36}$TbIG. This is 6 times larger than the magnetostriction of polycrystalline TbIG, and could account for the larger anisotropy of $Ce_{0.36}$TbIG compared to TbIG even if the actual value of magnetostriction is not as large as the extrapolated value.[13,45]

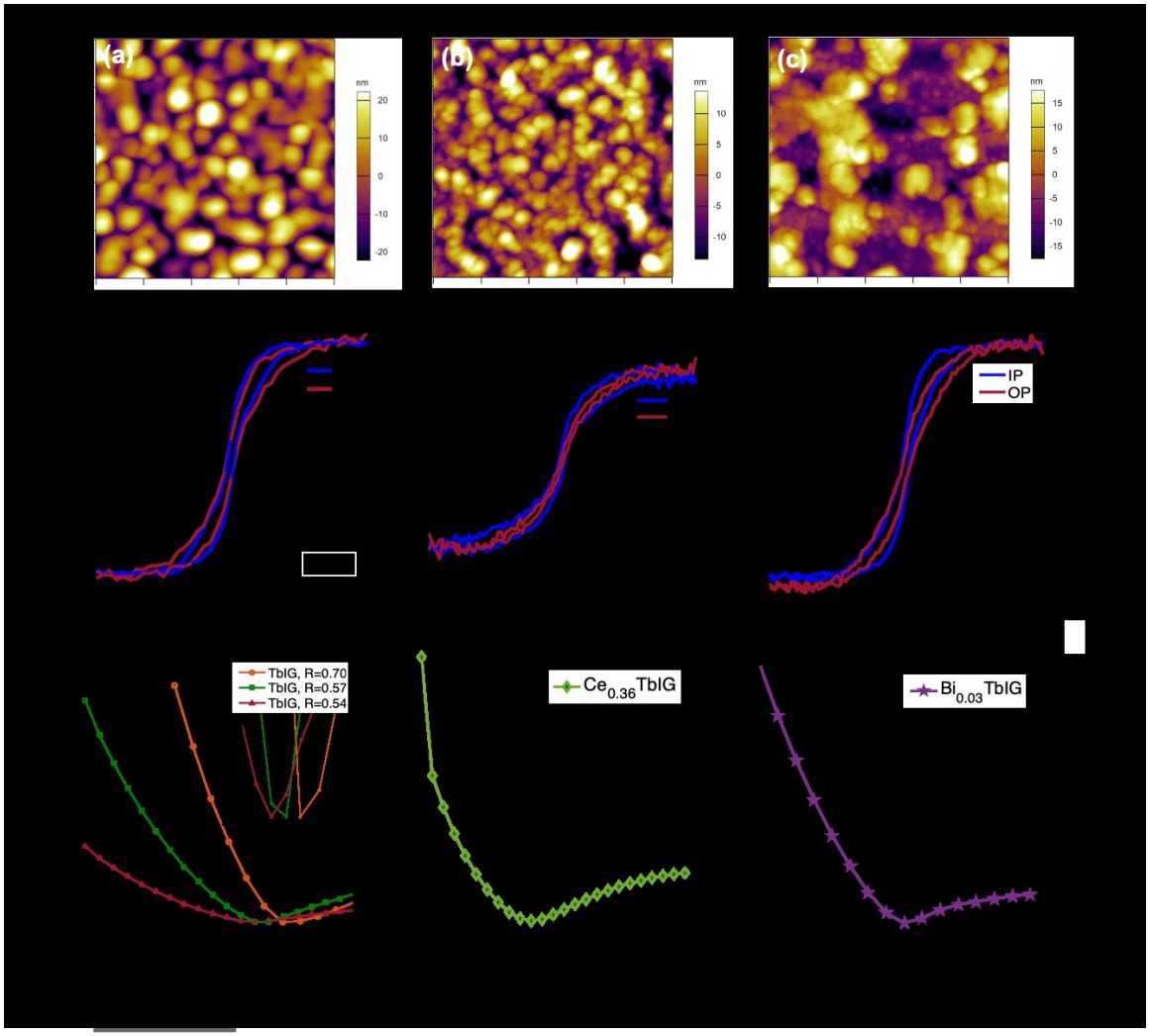

Figure 2. AFM height images post-RTA for (a) TbIG/Si (R=0.57), (b) $Ce_{0.36}$TbIG/Si (c) $Bi_{0.03}$TbIG/Si. In-plane (IP) and out-of-plane (OP) VSM room temperature hysteresis loops of (d) TbIG (R=0.57), (e) $Ce_{0.36}$TbIG and (f) $Bi_{0.03}$TbIG films on Si after RTA. Temperature dependent magnetization measured in a SQUID magnetometer for (g) TbIG (R=0.54, 0.57 & 0.7) , (h) $Ce_{0.36}$TbIG and (i) $Bi_{0.03}$TbIG.

Table 1. Magnetic, optical and magnetooptical properties of garnet films on Si

Sample	Calculated λ from Refs. 38, 42 (10^{-6})	Calculated K_{me} kJ/m^3	Calculated K_{sh} kJ/m^3	Calculated $K_u = K_{me} + K_{sh}$ kJ/m^3	Measured Anisotropy from anhysteretic loops kJ/m^3	Model T_{comp} (K)	Measured T_{comp} (K)	Faraday Rotation 1550 nm °cm^{-1}	Optical Loss 1550 nm dB.cm^{-1}	MO FoM 1550 nm °dB^{-1}
TbIG (95 nm) /Si, R=0.70	5.73	-2.8	-0.57	-3.37	-2.99	266	259.9 ± 2.5	3500 ± 300	19.9	175
TbIG (123 nm) /Si, R=0.57			-1.16	-3.96	-3.42	243	252.6 ± 2.5	5400 ± 600	17.4	310
TbIG (300 nm) /Si, R=0.54			-0.20	-3.00	-0.97	237	244.6 ± 2.4	1800 ± 240	-	-
$Bi_{0.03}$TbIG (80 nm) /Si	5.73	-2.8	-0.91	-3.71	-15.01	236	229.9 ±2.2	6200 ± 300	8.6	720
$Ce_{0.36}$TbIG (72 nm) /Si	35.4	-17.5	-0.42	-17.92	-9.09	193	145.8±1.4	4500 ± 100	8.3	540

We now describe the trends in magnetic compensation temperature with composition. In iron garnets the strongest superexchange interactions occur between the octahedral Fe^{3+} and tetrahedral Fe^{3+} sites leading to ferrimagnetic ordering. The moment of the rare earth (here Tb^{3+}) in the dodecahedral sites is coupled antiparallel to the tetrahedral Fe^{3+} as shown in Figure 1a. The dodecahedral Tb moments are canted at low temperatures around the [111] directions.[46,47] The different temperature-dependences of the Tb^{3+} and Fe^{3+} moments and the canting lead to a compensation temperature T_{comp} where the net Tb moment plus the octahedral Fe moment balances the tetrahedral Fe moment and the total moment is zero, i.e. at T_{comp} three dodecahedral Tb contribute the same net magnetic moment as one tetrahedral Fe^{3+}.

The polycrystalline TbIG (R=0.57) has a T_{comp} of 252.6 K [±2.5K] which is near the bulk T_{comp} of 248.6 K. [35] The iron deficient TbIG (R=0.70) has a T_{comp} of 260 K [±2.6K], while the iron rich

TbIG (R=0.54) has T_{comp} of 244.6 K [±2.4K] as shown in Figure 2g, which also demonstrates that an increase in Tb:Fe ratio raises the magnetization below T_{comp}. The increase in compensation temperature with Tb enrichment is similar to observations of Rosenberg et al. [35] and can be attributed to excess Tb occupying octahedral sites. Tb can also be tetravalent, and in Tb-rich TbIG the Tb^{4+} is more likely to occupy the smaller octahedral sites. When the Tb is on the octahedral sites it is expected to exhibit stronger exchange coupling to the Fe^{3+} and less canting than dodecahedral Tb. This raises the magnetic moment of the octahedral sublattice relative to that of the tetrahedral sublattice which increases T_{comp} and the low temperature net magnetization.

To compare with experimental data, a modified version of Dionne's molecular field coefficient model for garnets was employed. [48,49] The model was modified to account for off-stoichiometry in the films by assuming that excess rare-earth occupies the octahedral sites, whereas excess iron occupies the dodecahedral sites. The molecular field coefficients are assumed to be independent of the site occupancy. Comparison with experimentally measured compensation temperatures for the TbIG shows close agreement, with the trend of higher R values leading to higher compensation temperatures as shown in Figure S2.

Replacing Tb^{3+} ($4f^8$) with Bi^{3+} ($5d^{10}6s^2$) or Ce^{3+} ($4f^1$) is expected to reduce the magnetization of the dodecahedral sublattice and lower T_{comp}, with Bi having a larger effect than Ce. To estimate T_{comp} for $Ce_{0.36}$TbIG and $Bi_{0.03}$TbIG we assume that the contribution to the magnetic moment from the octahedral and tetrahedral Fe^{3+} is the same as that of YIG. [46,50-52] The Tb^{3+} sublattice magnetization can then be obtained by subtracting the magnetization of YIG[46] from that of TbIG,

$$[M_{Tb^{3+}}]_T = [M_{TbIG}]_T - [M_{YIG}]_T .$$

The resulting temperature-dependent sublattice magnetization of Tb^{3+}, $[M_{Tb^{3+}}]_T$, is then scaled to account for Bi^{3+} or Ce^{3+} substitution and added back to the temperature-dependent magnetization of YIG, $[M_{YIG}]_T$, to obtain the thermomagnetic curves for $Bi_{0.03}$TbIG and $Ce_{0.36}$TbIG. The predicted values of T_{comp} are shown in Table 1. The measured T_{comp} for $Bi_{0.03}$TbIG is lower than that of bulk TbIG by 19 K (Figure 2i), whereas the model predicted a decrease by 13 K. As a comparison, sol-gel $Bi_xTb_{3-x}IG$ showed a decrease in T_{comp} by 80 K for x=0.5. [28] In the case of $Ce_{0.36}$TbIG, the measured reduction in T_{comp} by 103 K (Figure 2h) is much larger than predicted by the model (56 K). A significant Ce^{4+} content appears unlikely, since it would be associated with Fe^{2+} and a higher optical absorption,[53] and there was no detectable CeO_2 found from XRD. The results show that both the Bi and Ce lower T_{comp} further than would be expected from a model based on simple dilution of the rare earth moment, which may indicate that the Ce or Bi affects the cation site occupancy in the films or the canting which is present at and below T_{comp}.[47]

2.3 Magneto-optical characterization

The temperature and spectral dependences of magneto-optical effects were obtained using a high precision magneto-optical spectrometer with a rotating analyzer, which enabled Faraday effect measurements to an accuracy of ~1 mdeg. Saturation Faraday rotation at 1550 nm at room temperature for the TbIG (R = 0.57), $Ce_{0.36}$TbIG and $Bi_{0.03}$TbIG films was 5400 ± 600 °/cm, 4500± 100 °/cm and 6200± 300°/cm respectively as shown in Figure 3a. The greater Faraday rotation of TbIG in comparison to YIG at energies around 1eV is due to strong optical transitions at higher energies induced by Tb^{3+}.[54] Tb^{3+} is reported to increase the splitting of oscillator strength for left and right circularly polarized light above 4e V in iron garnets due to exchange interactions between Tb^{3+} and tetrahedral Fe^{3+}[54]. The Faraday rotation of TbIG is thus proportional to the magnetic moment of the ions involved in this charge transfer process.[52,54] Bi^{3+} and Ce^{3+} both have a negative contribution to the Faraday rotation of YIG [55-57] and in $Ce_{0.36}$TbIG the positive Faraday rotation is lower in comparison to TbIG as expected. However, in $Bi_{0.03}$TbIG the Bi content is small and the Faraday rotation of TbIG and BiTbIG agree within the error range.

The polar Kerr rotation spectrum of the TbIG film shown in Figure 3b resembles prior results[54] for single crystal TbIG. In TbIG, optical transitions located between 3-4 eV originate from Fe^{3+} crystal-field transitions.[54] The amplitude of the Kerr effect is lower than the results of single crystals in Ref. [54]. Figure 3c shows longitudinal Kerr spectra of $Ce_{0.36}$TbIG at temperatures above and below T_{comp}. Below T_{comp} the octahedral Fe^{3+} and dodecahedral Tb^{3+} plus Ce^{3+} moments are oriented parallel to the field while the tetrahedral Fe^{3+} moments are antiparallel [58]. The Kerr rotation of the two datasets at 120 and 320 K have opposite signs as the orientation of the sublattices reverses at $T_{comp.}$ This change in sign is because the Kerr rotation like Faraday rotation is sensitive to the magnetic sublattices rather than the net magnetization [58,59]. $Ce_{0.36}$TbIG has a polar Kerr spectrum similar to that of single crystal CeYIG.[17] Figure 3d displays the temperature-dependent polar Kerr rotation of $Bi_{0.03}$TbIG at 2.5 eV. The change in sign indicates T_{comp} in the range of ~220 K, similar to the value of ~230 K found using SQUID magnetometry.

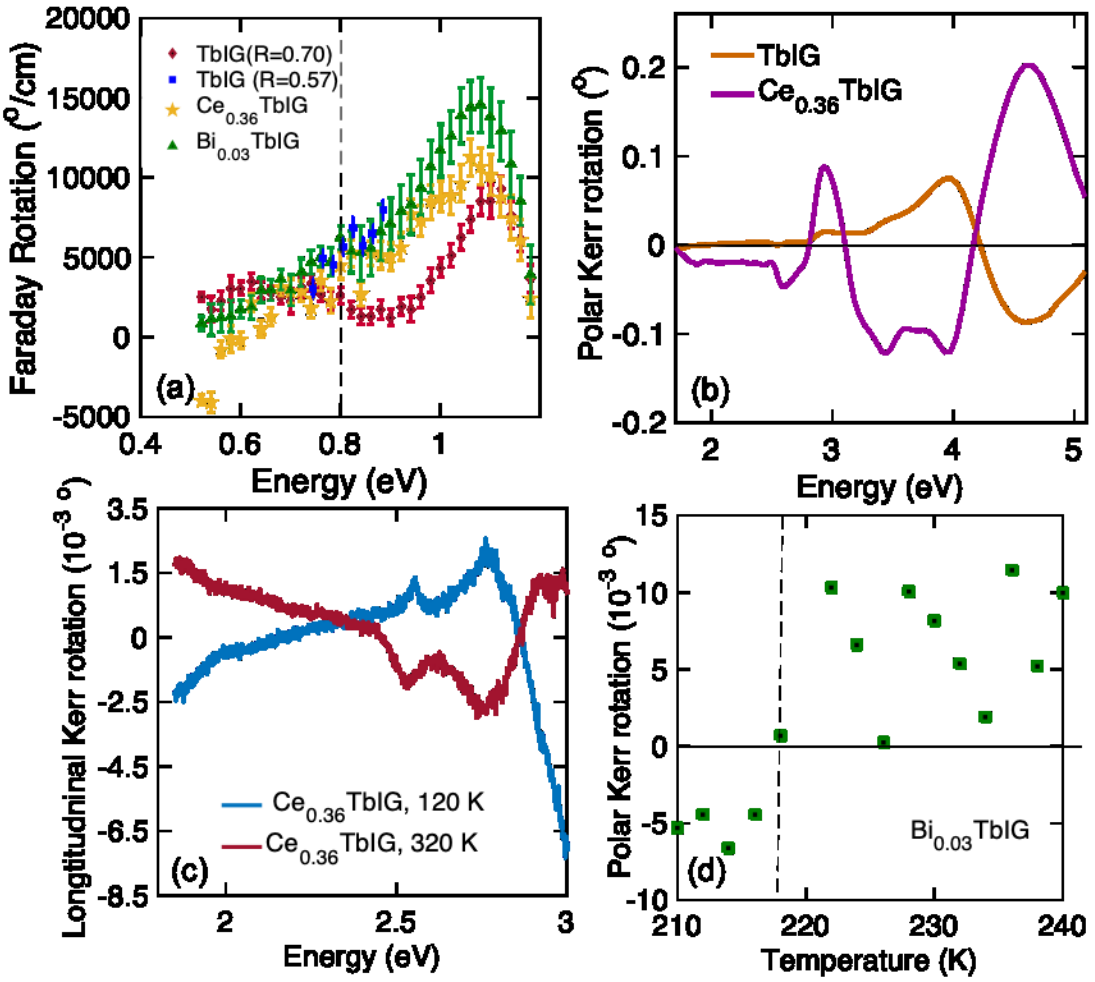

Figure 3. *(**a**) Room temperature Faraday rotation spectra of TbIG, $Ce_{0.36}$TbIG and $Bi_{0.03}$TbIG films (**b**) Room temperature polar Kerr rotation spectra of TbIG and $Ce_{0.36}$TbIG films. (c) Temperature-dependent longitudinal Kerr rotation of $Ce_{0.36}$TbIG. (d) Polar Kerr rotation versus temperature of $Bi_{0.03}$TbIG at energy 2.5eV, showing a sign change at T_{comp} in the range of ~220 K.*

4. Optical Characterization

A spectroscopic ellipsometer (J.A. Woollam RC2) was employed to acquire the spectra of the ellipsometric parameters PSI and DELTA. A set of three measurements at different angles of incidence were performed to enlarge the experimental dataset for subsequent fitting. For the fitting a model structure of a TbIG, $Ce_{0.36}$TbIG or $Bi_{0.03}$TbIG layer on an oxidized Si substrate was considered. The spectral dependence of complex refractive index (N = n+ik) of each garnet layer was parametrized by the sum of 4 Cody-Lorentz oscillators and their parameters were fitted together with the layer thickness and surface roughness. The resulting spectra of refraction

index and extinction coefficient, n and k, for the three TbIG, CeTbIG and BiTbIG samples are shown in Figure 4a and 4b and the spectrally dependent absorption coefficient is shown in Figure 4c. The spectral behavior of n and k in Figure 4a,b is typical for ferrimagnetic garnets [12,56,57,60,61] with the absorption edge around 2eV. We were unable to estimate the absorption of the 300 nm TbIG (R=0.54eV) film under 2eV from ellipsometric measurements, since this particular thickness leads to high interference in the low energy region and large depolarization. From Figure 4b one can see a slight red shift of the onset of absorption for Bi and Ce samples. The shift towards lower energies induced by increasing the amount of Bi in YIG is well reported. [56,62]

The CeTbIG and BiTbIG had lower absorption than the TbIG at 1550 nm as shown in Table 2. The absorption of TbIG at 1550 nm can be attributed to the tail extending from a Faraday rotation and optical absorption line at λ=1850 nm from inner 4f electronic transitions in the Tb^{3+} ion. [23,27,63] While rare earths predominately occur in the trivalent state, Tb^{3+} only has one electron above the half-filled 4f shell and therefore is known to readily oxidize to Tb^{4+}, especially in cubic materials. [35,64-66] Tb^{4+} has been reported to be a quenching site of fluorescence for its strong and broad absorption in the visible region.[62] High resolution XPS data from the TbIG, CeTbIG and BiTbIG films shows the presence of Tb^{4+} in all three films, Figure 4(e) which is in accordance with results from single crystal TbIG films [35]. The higher intensity of the Tb^{4+} peak can be qualitatively interpretated as a larger proportion of Tb^{4+} than Tb^{3+} in these films. [35,67] Moreover, the intensity of Tb^{4+} relative to Tb^{3+} peaks was stronger in the TbIG film compared to $Ce_{0.36}$TbIG and $Bi_{0.03}$TbIG films pointing towards a higher fraction of Tb^{4+} in TbIG compared to the other two films. The XPS spectra of Fe 2p in TbIG reveal a shift to a lower binding energy compared to the $Ce_{0.36}$TbIG and $Bi_{0.03}$TbIG films. A shift to lower binding energy of the Fe $2p_{3/2}$ peak in Fe_3O_4 has been associated with a reduction of Fe^{3+} to Fe^{2+} [68] due to the lower binding energies associated with Fe^{2+} compounds than Fe^{3+} compounds [68,69]. This higher amount of Fe^{2+} in the TbIG films correlates with the higher amount of Tb^{4+}, and has been reported in other rare earth iron garnets as a result of the presence of tetravalent ion impurities. [63,70-72] The presence of Fe^{2+} in iron garnets results in enhanced absorption due to the relaxation of Fe^{3+} - Fe^{2+} where an electron promoted by a photon in Fe^{2+} transfers to a nearby Fe^{3+} ion. This relaxation process is associated with a large change in dipole moment and strong absorption, and at high concentrations of tetravalent ions the absorption is reported to be proportional to the amount of tetravalent ions (here Tb^{4+}) because they increase the number of Fe^{2+} ions. [63,70]

In addition to Fe^{3+}-Fe^{2+} relaxation, the simultaneous presence of Tb^{4+} and Tb^{3+} can also affect the optical properties of the garnet films. [64] The electron donor behavior of Tb^{3+} allows electronic transitions from 4f → 4f and 4f→5d between 1.2 and 6eV while the electron acceptor behavior of Tb^{4+} allows charge transfer from ligand orbitals to rare earth or Fe^{3+} ions. [64] These additional absorption pathways result in TbIG having higher absorption than YIG or BiYIG. [12] However, we find moderate additions of Ce^{3+} and very small additions of Bi^{3+} are able to reduce this absorption to less than half as shown in Table 1 and also depicted in Figure 4c. The Bi^{3+} and Ce^{3+} ions are associated with lower amounts of Tb^{4+} and Fe^{2+} as indicated by XPS, lowering the absorption coefficient significantly. Nonetheless, the TbIG (R=0.57) has a good MO FoM of 310 $°dB^{-1}$ compared to the FoM of 38 $°dB^{-1}$ for polycrystalline CeYIG. [12] As a result of having both a lower absorption than TbIG albeit a slightly smaller Faraday rotation due to the negative

contribution of Ce^{3+}, the $Ce_{0.36}$TbIG film has a FoM almost 2 times higher than that of TbIG. $Bi_{0.03}$TbIG triumphs with a FoM of 720°dB^{-1}as shown in Figure 4c. The small amount of Bi^{3+} does not negatively impact the Faraday rotation but it reduces the optical absorption significantly. So far, the highest FoM of 769°dB^{-1} was reported[12] for polycrystalline BiYIG with a 40 nm bottom YIG seed layer, and the $Bi_{0.03}$TbIG in this work has the advantage of having a similarly high FoM while allowing for simpler fabrication and better device performance by eliminating the seed layer.

Conclusion

TbIG, CeTbIG and BiTbIG films were grown directly on Si via PLD without a seed layer. The films exhibit the highest reported Faraday rotation for polycrystalline films at 1550 nm wavelength, up to 6200 °/cm for $Bi_{0.03}$TbIG films and a similar value for TbIG. Despite its high Faraday rotation, the TbIG films exhibited an higher optical absorption than that of CeTbIG and BiTbIG, attributed to both the greater concentration of Tb^{4+} and Fe^{2+} that can facilitate absorption through Fe^{3+}-Fe^{2+} relaxation and charge transfer from ligand orbitals, and the 4f electronic transitions of Tb^{3+}. Addition of Ce and Bi lowered the absorption significantly by reducing absorption pathways related to the presence of Tb^{4+}, thus improving the overall FoM of these films. This work emphasizes the critical importance of controlling the Tb^{3+}/Tb^{4+} ratio, analogous to the improvement in MO performance obtained by controlling Ce^{4+} in CeYIG via growth conditions [73]. The high FoM and the single layer growth process make Ce and especially Bi-substituted TbIG attractive materials for integrated nonreciprocal photonic devices or for other applications requiring magnetooptical materials such as magnetophotonic crystals or other nonreciprocal magnetooptical metamaterials. [74,75]

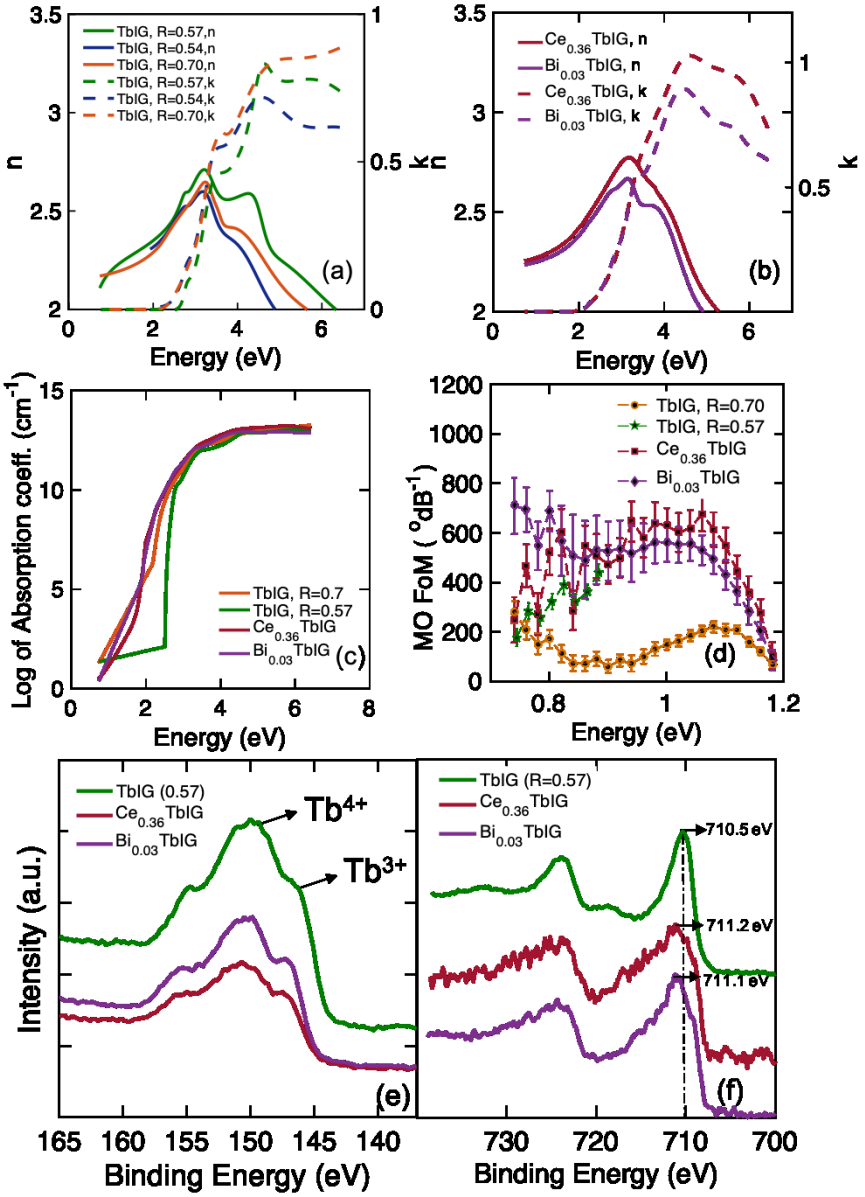

Figure 4*. Refractive index (n) and extinction coefficient (k) spectra of (a) TbIG (R=0.54, 0.57, 0.7), (b) $Ce_{0.36}$TbIG and $Bi_{0.03}$TbIG films. (c) Spectral dependence of absorption coefficient of TbIG, $Ce_{0.36}$TbIG and $Bi_{0.03}$TbIG films. (d) MO figure of merit (FoM) versus energy for TbIG (R=0.57,0.7) , $Ce_{0.36}$TbIG and $Bi_{0.03}$TbIG films. High resolution XPS spectra of (e) Tb 4d and (f) Fe 2p of the TbIG (R=0.57) , $Ce_{0.36}$TbIG and $Bi_{0.03}$TbIG films.*

Acknowledgement

TF and CAR gratefully acknowledge support of NSF ECCS 2028199, Micron Foundation and Draper Laboratories. This work made use of the Shared Experimental Facilities supported in part by the MRSEC Program of the National Science Foundation under award number DMR 1419807. The support of Czech Ministry of Education (grant No. LTAUSA18176) is also acknowledged. The authors are grateful to MIT Shared Facilities staff, particularly Alan Schwartzman for help and guidance in collecting and analyzing AFM data.

Experimental Methods

Thin Film Growth: TbIG, CeTbIG and BiTbIG films were grown on Si substrates by PLD from targets of composition $Tb_3Fe_5O_{12}$, $Ce_1Tb_2Fe_5O_{12}$ and $Bi_{0.3}Tb_{2.7}Fe_5O_{12}$ using a 248 nm wavelength 45 KrF excimer laser (Coherent, COMPex Pro 205). The targets were prepared by mixed oxide sintering [12] of 99.999% pure Tb_2O_3, CeO_2, Bi_2O_3, and Fe_2O_3 powders. The films were grown at a repetition rate of 10 Hz and laser fluence of 1.5 and 2.5 J cm^{-2}. The substrate heater setpoint temperature was 900°C which corresponds to a substrate temperature of approximately 750 ˚C, and an oxygen pressure of 10 mTorr. Afterwards the films were rapid thermally annealed (RTA) at 900 °C for 3 minutes in oxygen. Different compositions for the CeTbIG and BiTbIG films were achieved by codeposition with the TbIG target, by alternately ablating the targets using 25 laser shots on TbIG target and between 4-15 laser shots on the CeTbIG and BiTbIG targets.

Material characterization: θ–2ω diffraction data of the polycrystalline films were carried out using a PANalytical X'pert Pro MPD diffractometer. Compositional analysis was done by wavelength dispersive spectroscopy (WDS) using a JEOL-JXA-8200 Superprobe. The cation ratios in the thin films were calculated using GMR electron probe thin film microanalysis program[76] which takes into account the substrate contributions to the WDS spectrum and the effect of the substrate-film interface. Atomic force microscopy (AFM) measurements were performed using a Cypher-S AFM, equipped with blueDrive (Asylum Research, an Oxford Instruments company). The bimodal technique, called DualAC, was employed for high quality images of the lateral microstructure of the thin films. Also, the photothermal excitation technique, called blueDrive, was utilized to tune both the primary and second order resonance peaks. In particular, the signal from the minute amplitude of oscillation of the second mode for an Olympus AC160TSA-R3 cantilever is used to present the AFM images in the supplementary Figure S1. The thickness was measured by surface profilometry on a KLA-Tencor P-16+ stylus profiler. Room temperature magnetic properties were characterized by vibrating sample magnetometry (VSM) using an ADE Technologies VSM Model 1660. Temperature dependent magnetic characterization was performed using Quantum Design's Magnetic Properties Measurement System (MPMS 3) that allows measurements in the temperature range 1.8 to 400 K with magnetic fields up to -70 kOe and temperature accuracy specification of better than +/- 1% at low temperatures. Spectroscopic ellipsometry was performed on a J.A. Woollam RC2 ellipsometer for three light incident angles ranging from 55° to 65°. The experimental data were processed using proprietary software CompleteEase by J.A Woollam. Room temperature Faraday magneto-optical spectra were collected by a spectrometer based on the compensation method and utilizing a rotating polarizer approach to modulate the detected signal for the synchronous detection. The light from the highly stabilized bulb was monochromated, passed through the sample at normal incidence, then detected by a PbS detector. The applied magnetic field from the electromagnet was 0.7 T, which was sufficient for magnetic saturation of the samples. Kerr magneto-optical spectra were acquired by spectrometer using the rotating analyzer method with a laser driven lamp and CCD detector. The magnetic field was 1 T.

References

[1] H. Dötsch, N. Bahlmann, O. Zhuromskyy, M. Hammer, L. Wilkens, Gerhardt, R. Hertel, P. Hertel and A.F. Popkov, J. Opt. Soc. Am. B **2005,** 22, 240.

[2] T. Haider, *Int. J. of Electromagnetics App.* **2017**, *7*, 17.

[3] T. Mizumoto, R. Baets, J.E. Bowers, *MRS Bulletin*, **2018**, *43*, 419.

[4] B. J. Stadler, T. Mizumoto, *IEEE Photonics J.* **2013**, *6*, 1.

[5] Q. Du, T. Fakhrul, Y. Zhang, J. Hu, C. A. Ross. *MRS Bull.* **2018**, *43*, 413.

[6] Y. Shoji, T. Mizumoto, *Sci. Technol. Adv. Mater.* **2014**, *15*, 014602.

[7] D. Huang, P. Pintus, J. E. Bowers, *Opt. Mater. Express **2018**, 8*, 2471

[8] Y. Zhang, Q. Du, C. Wang, T. Fakhrul, S. Liu, L. Deng, D. Huang, P. Pintus, J. Bowers, C.A. Ross, J. Hu, Opt. ***2019***, *6*, 473.

[9] P. Hansen, K. Witter, W. Tolksdorf , *Phys. Rev. B* **1983**, *27*, 6608.

[10] L. Bi, J. Hu, P. Jiang, D. H. Kim, G. F. Dionne, L. C. Kimerling, C. A. Ross, *Nat. Photonics* **2011**, *5*, 758.

[11] Q. Du, C. Wang, Y. Zhang, Y. Zhang, T. Fakhrul, W. Zhang, C. Goncalves, C. Blanco, K. Richardson, L. Deng, C.A. Ross, L. Bi, J. Hu, *ACS Photonics* **2018**, *5*, 5010.

[12] T. Fakhrul, S. Tazlaru, L. Beran, Y. Zhang, M. Veis, C.A. Ross, Adv. Opt. Mat. **2019**, 7, 1900056.

[13] X. Y. Sun, Q. Du, T. Goto, M. C. Onbasli, D. H. Kim, N. M. Aimon, J. Hu, C.A. Ross, *ACS Photonics* **2015**, *2*, 856.

[14] L. Bi, J. Hu, P. Jiang, H. S. Kim, D. H. Kim, M. C. Onbasli, G. F. Dionne, C. A. Ross, *Materials **2013**,* 6, 5094.

[15] J. Hu, Y. Zhang, Q. Du, C. Wang, T. Fakhrul, Y. Zhang, S. Liu, L. Deng, C. Goncalves, C. Blanco, K. Richardson in Proc. SPIE 11289, *Photonic and Phononic Properties of Engineered Nanostructures X*, San Francisco, CA, **2020**.

[16] T. Goto, M. C. Onbaşlı, C. A. Ross. **2012.** *Opt. Exp*ress 2012, *20*, 28507.

[17] M.C. Onbasli, L. Beran, M. Zahradník, M. Kučera, R. Antoš, J. Mistrík, G. F. Dionne, M. Veis, C. A. Ross, *Sci. Rep.* **2016**, *6*, 23640.

[18] Y. Yoshimoto, T. Goto, R. Isogai, Y. Nakamura, H. Takagi, C.A. Ross, M. Inoue, *Opt. express* **2016**, *24*, 8746.

[19] J.J. Bauer, J.J., E.R. Rosenberg, S. Kundu, K.A. Mkhoyan, P. Quarterman, A.J. Grutter, B.J. Kirby, J.A. Borchers, C.A. Ross, *Adv. Electron. Mater.* ***2020***, *6*, 1900820.

[20] Y. Zhang, Q. Du, C. Wang, W. Yan, L. Deng, J. Hu, C.A. Ross, L. Bi , *APL Mater.* **2019**, *7*, 081119.

[21] J.W. Nielsen, E.F. Dearborn, *J. Phys. Chem. Solids* **1958** , *5*, 202.

[22] R. Wang, C. Yang , M. Fan, M. Wu, C. Wang, X. Yu, J. Zhu, J. Zhang, G. Li, Q. Huang, D. Chen, T. Jin, T. Kamiyama, F. Liao, J. Lin, *J. Alloys Compd.* 2013, 554, 385.

[23] T. Tamaki, H. Kaneda, N. Kawamura, *J. Appl. Phys.* **1991**, *70*, 4

[24] H. Umezawa, Y. Yokoyama, N. Koshizuka, *J. Appl. Phys*. **1988,** *63*, 3113.

[25] Y. Honda, T. Ishikawa, T. Hibiya, *J. Magn. Soc. Jpn* **1987**, *11*, 361.

[26] M. Guillot, H. L. Gall, J.M. Desvignes, M. Artinian, *IEEE Trans. Magn.* **1994**, *30*, 4419.

[27] V.J. Fratello, S.J. Licht, C.D. Brandle, *IEEE Trans. Magn*. **1996**, *32*, 4102.

[28] I.J. Park, K.U. Kang, C.S. Kim, *IEEE Trans. Magn.* **2006**, *42*, 2882.

[29] P. Dulal, A. D. Block, T. E. Gage, H.A Haldren, S. Y. Sung, D. C. Hutchings, B. J. H. Stadler, *ACS Photonics* **2016**, *3*, 1818.

[30] A.D. Block, P. Dulal, B.J.H. Stadler, N.C.A. Seaton, IEEE Photonics J. 2014, 6, 1.

[31] K. Srinivasan, C. Zhang, P. Dulal, C. Radu, T.E. Gage, D.C. Hutchings, B.J.H. Stadler, ACS Photonics **2019**, *6*, 2455.

[32] K. Srinivasan, C. Radu, D. Bilardello, P. Solheid, B.J. H Stadler, *Adv. Funct. Mater*. **2020**, 30, 2000409.

[33] P. Dulal, T.E. Gage, A.D. Block, E. Cofell, D.C. Hutchings, B.J.H Stadler in Proc. IEEE Photonics Conference, IEEE, Waikoloa, HI, **2016**.

[34] K. Srinivasan, T.E. Gage, B.J.H. Stadler in Proc. Conference on Lasers and Electro-Optics, Science and Innovations, San Jose, CA, **2018**.

[35] E.R. Rosenberg, L. Beran, C.O. Avci, C. Zeledon, B. Song, C.F. Gonzalez, J. Mendil, P. Gambardella, M. Veis, C. Garcia, G.S. Beach, Phys. Rev. Mat. **2018**, *2*, 094405.

[36] A.E. Clark, R.E. Strakna,*J. Appl. Phys.* **1961**, *32*, 1172.

[37] S. Iida, *J. Phys. Soc. Jpn*, **1967**, *22*, 1201.

[38] N.S Akulov, J. *Phys.* **1930**, *66*, 533.

*[39] H. B. Callen, N. Goldberg, J. Appl. Phys. **1965**, 36, 976.*

[40] J.J. Bauer, E.R. Rosenberg, C.A. Ross, *Appl. Phys. Lett.* **2019**, *114*, 052403.

[41] S. Geller, G. P. Espinosa, P. B. Crandall, *J. Appl. Crystallogr.* **1969**, *2*, 86.

[42] S.H. Lim, M. Murakami, W.L. Sarney, S.Q. Ren, A. Varatharajan, V. Nagarajan, S. Fujino, M. Wuttig, I. Takeuchi, L.G. Salamanca-Riba, *Adv. Funct. Mater.* **2007**, *17*, 2594.

[43] H. P. J. Wijn, *Garnets* (Springer-Verlag, Berlin, Heidelberg, 1991), Vol. 27e.

[44] R.L. Comstock, J..J. Raymond, J. Appl. Phys. **1967**, 38, 3737.

[45] E. Lage, L. Beran, A.U. Quindeau, L. Ohnoutek, M. Kucera, R. Antos, S.R. Sani, G.F. Dionne, M. Veis, C.A. Ross, *APL Mater. **2017**, 5*, 036104.

[46] G.F. Dionne, *Magnetic oxides*, Springer, NY **2009**.

[47] Y.J. Hong, J.S. Kum, I.B. Shim, C.S. Kim, IEEE Trans. Magn. 2004, 40, 2808.

[48] G. F. Dionne, J. Appl. Phys. 1970, 41, 4874.

[49] G.F. Dionne, *J. Appl. Phys. 1976*, *47*, 4220.

[50] M. Guillot, H. L. Gall, *J. Phys*. (Paris) **1977**, *38*, 871.

[51] G.Y. Zhang, X.W. Xu, T.C. Chong, *J. Appl. Phys.* **2004,** *95*, 5267.

[52] W.A. Crossley, R.W. Cooper, J.L. Page, R.P.V. Stapele, *Phys. Rev.* **1969,** *181*, 896.

[53] X. Liang, J. Xie, L. Deng, L. Bi, *Appl. Phys. Lett.* **2015**, *106*, 052401.

[54] N.P. Thuy, Š. Višňovský, V. Prosser, R. Krishnan, T.K. Vien, *J. Appl. Phys*, 1981, *52*, 2292.

[55] S. Wittekoek, T. J. Popma, J. M. Robertson, P. F. Bongers, *Phys. Rev. B* **1975**, *12*, 2777.

[56] M. Kucera, J. Bok, K. Nitsch, *Solid State Commun. 1989*, *69*, 1117.

[57] P. Hansen, J. P. Krumme, *Thin Solid Films* **1984**, *114*, 69.

[58] A. K. Zvezdin, V. A. Kotov, *Modern Magnetooptics and Magnetooptical Materials,* CRC press, FL, **1997**.

[59] K. Ganzhorn, J. Barker, R. Schlitz, B. A. Piot, K. Ollefs, F. Guillou, F. Wilhelm, A. Rogalev, M. Opel, M. Althammer, S. Geprägs, H. Huebl, R. Gross, G. E. W. Bauer, and S. T. B. Goennenwein, Phys. Rev. B **2016**, 94, 094401.

[60] G. F. Dionne, G. A. Allen, *J. Appl. Phys.* **1993**, *73*, 6127

[61] G. B. Scott, D. Lacklison, *IEEE Trans. Magn.* **1976**, *12*, 292.

[62] E. Jesenska, T. Yoshida, K. Shinozaki, T. Ishibashi, L. Beran, M. Zahradnik, R. Antos, M. Kučera, M. Veis, *Opt. Mater. Express* 2016, *6*, 1986.

[63] D.L. Wood, J.P. Remeika, *J. Appl. Phys.* **1967**, *38*, 1038.

[64] R.K. Verma, K. Kumar, S.B. Rai, *Solid State Sci.* 2010, *12*, 1146.

[65] D.Y. Lu, Solid State Ionics **2015**, 276, 98.

[66] H. Ebendorff-Heidepriem, D. Ehrt, . *J. Phys. : Condens. Matter **1999**, 11*, 7627.

[67] K.I. Gnanasekar, A.S. Tamhane, R. Pinto, R. Nagarajan, M. Sharon, L.C. Gupta, and R. Vijayaraghavan, *Appl. Phys. Lett.* **1994** , *219*, 183.

[68] P. Mills, J.L. Sullivan, J. Phys. D: Appl. Phys. **1983**,*16*, 723.

[69] G.C. Allen, M.T. Curtis, A.J. Hooper, P.M. Tucker, J. Chem. Soc., Dalton Trans. **1974**,14, 1525.

[70] D.L. Wood, J.P. Remeika, *J. Appl. Phys.* **1966**, *36*, 1232.

[71] R.A. Lefever, A.B. Chase, J. Chem. Phys. **1960**, 32,1575.

[72] K.A. Wickersheim, R.A. Lefever, *J. Chem. Phys.* **1962**, *36*, 844.

[73] Y. Zhang, C.T. Wang, X. Liang, B. Peng, H.P. Lu, P.H. Zhou, L. Zhang, J.X. Xie, L.J. Deng, M. Zahradnik, L. Beran, M. Kucera, M. Veis, C.A. Ross, L. Bi, *J. Alloys Compd.* **2017**, 703, 591.

[74] Ignatyeva, D.O., Karki, D., Voronov, A.A., Kozhaev, M.A., Krichevsky, D.M., Chernov, A.I., Levy, M. and Belotelov, V.I., Nature Communications, **2020**. 11(1), pp.1-8.

[75] Arthur R. Davoyan, Ahmed M. Mahmoud, and Nader Engheta, Opt. Express **2013** 21(3), 3279-3286

[76] R.A.Waldo, Microbeam Anal. **1988**, 23, 310.

Table of Contents Graphic and Text

This article presents developments in the integration of high figure-of-merit (FoM) magneto-optical (MO) rare earth garnet films on to silicon for use in optical isolators. TbIG, $Ce_{0.36}$TbIG and $Bi_{0.03}$TbIG garnet thin films are grown on Si substrates by pulsed laser deposition. The films have a Faraday rotation that is almost twice as high as previous reports for polycrystalline MO garnet films. $Ce_{0.36}$TbIG and $Bi_{0.03}$TbIG exhibited lower optical absorption than TbIG, attributed to a reduction in Fe^{2+} and Tb^{4+} absorption pathways. The MO FoM of $Bi_{0.03}$TbIG is 720 $^{o}dB^{-1}$, similar to that of BiYIG films but without the need for a YIG seedlayer for integration.

Keywords: Rare-earth iron garnets, magneto-optical, optical absorption, figure of merit,